Quality analysis of Worldview-4 DSMs generated by least squares matching and semiglobal matching

Umut G. Sefercik,[a] **Mehmet Alkan**,[b,*] **Karsten Jacobsen**,[c] **Can Atalay**,[d] **and Gurcan Buyuksalih**[e]

[a]Gebze Technical University, Department of Geomatics Engineering, Kocaeli, Turkey
[b]Yildiz Technical University, Department of Geomatics Engineering, Istanbul, Turkey
[c]Leibniz University Hannover, Institute of Photogrammetry and Geoinformation, Hannover, Germany
[d]Zonguldak Bülent Ecevit University, Department of Geomatics Engineering, Zonguldak, Turkey
[e]Private Sector, Istanbul Metropolitan Municipality, Istanbul, Turkey

Abstract. For the estimation of a dense disparity map from a rectified space-borne stereo image pair and generation of the most qualified digital surface model (DSM), new image matching algorithms are being developed. Our study has two main goals of the DSM quality validation of Worldview-4 (WV-4), which offers the highest ground sampling distance (GSD) (30 cm) of civilian optical space-borne missions together with Worldview-3 (WV-3), and performance comparison of semiglobal matching (SGM) and least squares matching (LSM), two of the most preferred image matching algorithms for space-borne data. In the Istanbul study area with a rough topographic structure, 1 m gridded DSMs were derived from geometrically corrected WV-4 stereo image pairs. The qualities were estimated by well-rounded visual and statistical approaches based on standard deviation and normalized median absolute deviation. In model-to-model comparisons, a very high-resolution airborne laser scanning (ALS) DSM was utilized as the reference model. The results demonstrated that the WV-4 DSM derived by SGM has the standard deviation of ± 0.51 m (1.7 GSD) in height in open areas, whereas the LSM DSM has ± 1.46 m. In addition, the visual quality of SGM is much better than LSM through building description potential. © *2021 Society of Photo-Optical Instrumentation Engineers (SPIE)* [DOI: 10.1117/1.JRS.15.034515]

Keywords: Worldview-4; least squares matching; semiglobal matching; digital surface model; quality.

Paper 210209 received Apr. 7, 2021; accepted for publication Aug. 9, 2021; published online Aug. 23, 2021.

1 Introduction

In recent years, by force of rapid developments in remote sensing technology, high-resolution digital surface models (DSMs) and digital three-dimensional (3D) cartographic representation of all-natural and human-made objects in a target area became the most beneficial and indispensable products for a large variety of applications such as 3D city modeling,[1] the establishment of geographical information systems,[2] fusion approaches in space-borne automatic object extraction,[3] disaster monitoring and management,[4] generation of forest stand height maps,[5] and detection and monitoring of archaeological and cultural heritage sites.[6]

Spatial resolution is the most significant parameter for describing the 3D visible surface of the DSM's target area as close to the real surface as possible. In the last decade, with valuable contributions of DigitalGlobe, the spatial resolution of optical space-borne missions was improved, and the "very high-resolution (VHR ≤ 0.5 m)" concept entered space-borne remote sensing technical glossary in 2007 with Worldview-1 mission.[7] Beginning with WV-1, DigitalGlobe continued with a series of commercial Earth-imaging satellites increasing the

*Address all correspondence to Mehmet Alkan, alkan@yildiz.edu.tr

1931-3195/2021/$28.00 © 2021 SPIE

Downloaded From: https://www.spiedigitallibrary.org/journals/Journal-of-Applied-Remote-Sensing on 05 Jan 2022
Terms of Use: https://www.spiedigitallibrary.org/terms-of-use

spatial resolution and Worldview-4 (WV-4); the latest member of the Worldview series was successfully launched in November 2016. WV-4 presents 0.31 m panchromatic (PAN) and 1.24 m multispectral (MS) imaging resolutions from a 617 km orbital height at nadir view. In principle, VHR provides a qualitative leap in the space-borne missions' performance indices such as geolocation accuracy and mapping capability.[8,9] The geolocation accuracy of WV-4 is specified as <5 m considering CE90 without ground control points (GCP) by DigitalGlobe. For high-quality mapping, the satellite has PAN + 4 MS bands as red, green, blue, and near-infrared with an 11-bits dynamic range. To improve the geolocation accuracy and mapping quality of VHR satellite imagery, the literature mainly investigates the effect of image matching algorithms and different image orientation models such as deterministic models and rational function models.[10–12] Accordingly, some research on the orthorectification and DSM qualities of Worldview-2 (WV-2) and Worldview-3 (WV-3)[9,13–17] exists. However, due to being the latest VHR Worldview mission, there is no comprehensive investigation of WV-4 geolocation accuracy and DSM quality in the literature. In this study, we have two aims: the comprehensive investigation of the WV-4 DSM potential and the comparison of least squares matching (LSM)[18] and semiglobal matching (SGM)[19] effects on WV-4 DSM quality. The building monitoring performances of LSM and SGM DSMs generated from 1 m resolution IKONOS stereo imagery was compared in Ref. 20, and the authors achieved better results with SGM. In Ref. 21, the effect of image-matching methods in DSM generation was also investigated with IKONOS data. In this study, the potential of generated WV-4 DSMs is evaluated by detailed model-to-model visual and statistical approaches using a reference airborne laser scanning (ALS) DSM. With the advantage of high-resolution and accurate point clouds, the ALS technique enables the generation of high-quality realistic DSMs of the target areas and is preferred as the reference data for many kinds of applications. In Ref. 22, the ALS DSM was used as the reference data to validate the DSM derived from the unmanned air vehicle structure from motion technique. In Ref. 23, accuracy of global TanDEM-X radar DSM was assessed using reference ALS DSM as well. In Ref. 24, the accuracy of SRTM and ASTER DSMs was also analyzed with ALS reference DSM.

This paper is organized as follows: characteristics of the study area and analyzed WV-4 images are given in Sec. 2. The image orientation, LSM and SGM techniques, and DSM generation and validation methodologies are described in Sec. 3. The achieved results are presented in Sec. 4 and discussed in Sec. 5, followed by the conclusions.

2 Characteristics of the Study Area and Analyzed WV-4 Images

Kilyos, a study area located in the northern part of Istanbul, has a shoreline with the Black Sea. Three classes dominate the land cover: built-up, open, and forest. The land surface is rolling, and the orthometric heights are between 0 and 100 m. Figure 1 presents the study area, land cover classes, and terrain slope.

Many limiting factors, especially the acquisition geometry of space-borne images, have significant effects on height accuracy. In theory, the main components of height accuracy are the standard deviation of the x-parallax (Spx) and the height to base ratio (h/b) [Eq. (1)]. A smaller angle of convergence leads to better similarity of the matched images, which reduces the Spx.[25] The characteristics and acquisition geometry of used WV-4 optical stereo images are given in Fig. 2. The images have a 1 min 8 sec acquisition interval. The WV-4 satellite has not captured new images since January 2019 because of a failure in its control moment gyros. However, the satellite's archive images are in demand through having the highest spatial resolution ever:

$$SZ = \mathrm{Spx} \times \frac{h}{b}. \tag{1}$$

3 Methodology

For the generation and validation of WV-4 DSMs, the following methodologysteps, shown in Fig 3, was applied. Two WV-4 DSMs were generated with LSM and SGM algorithms and comprehensively analyzed separately. These processing steps are given in three sections as image orientation, DSM generation by LSM and SGM, and DSM validation.

Downloaded From: https://www.spiedigitallibrary.org/journals/Journal-of-Applied-Remote-Sensing on 05 Jan 2022
Terms of Use: https://www.spiedigitallibrary.org/terms-of-use

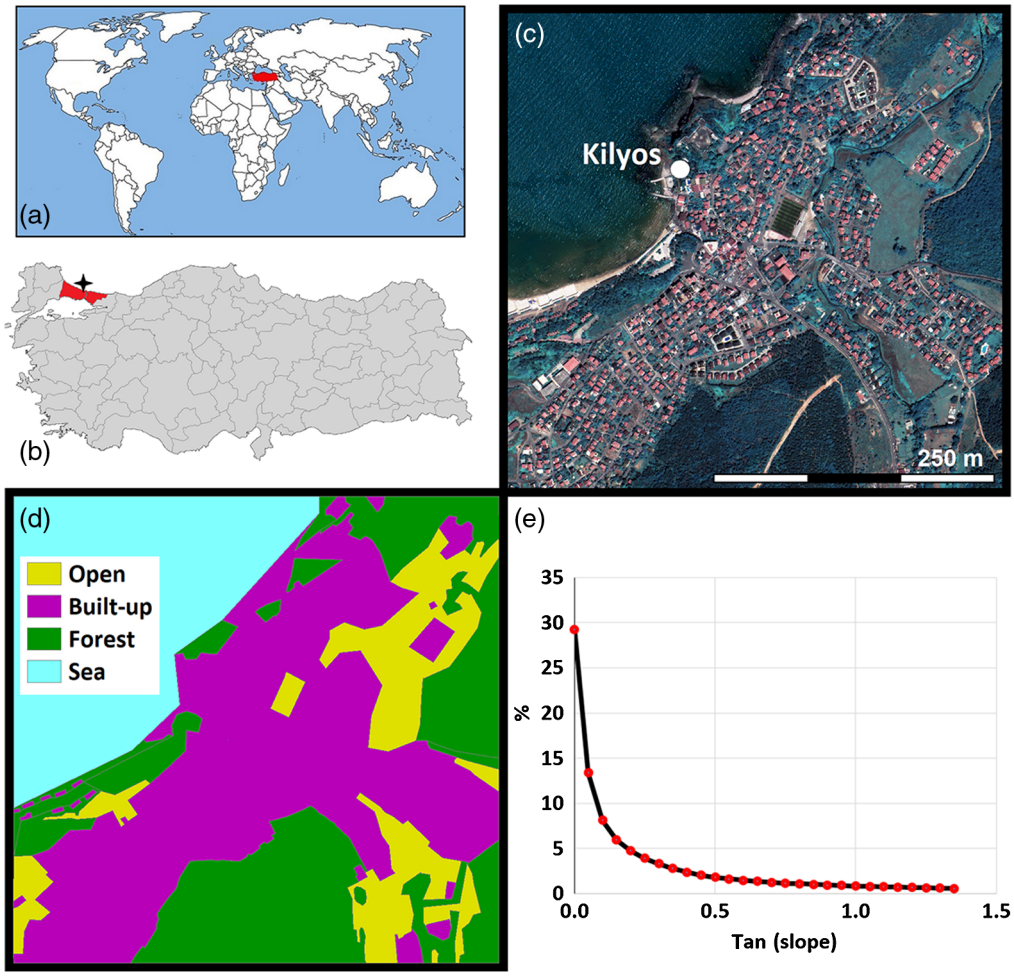

Fig. 1 Study area: (a) Turkey on world map, (b) study area on Turkey, (c) study area on WV-4 image, (d) study area land cover classes, and (e) study area terrain slope map.

Characteristics	Image 1	Image 2	Imaging geometry
Used imaging band	PAN + MS + NIR		
Product type and mode	Stereo / Full swath		
Acquisition date	24.06.2017		
Acquisition time (h:m:s)	08:56:15.02	08:57:23.28	
Map projection and zone	UTM Zone 35		
Coverage	100 km^2		
Pixel size (Row×Column)	68616×25604 PAN / 17154×6401 MS		
Spatial resolution (at nadir)	0.31 m PAN / 1.24 m MS		
Radiometric level	Corrected		
Radiometric resolution	16 bit		
Scan direction	Forward		
Base length	375898 m		
Height to base relation	1 : 1.20		

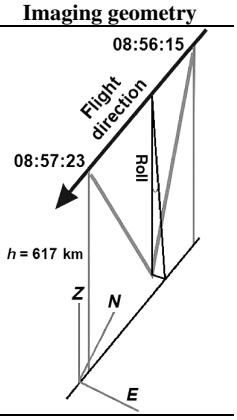

Fig. 2 Characteristics and the acquisition geometry of WV-4 stereo images.

3.1 *Image Orientation*

The DigitalGlobe specifies the horizontal and vertical geolocation accuracies of the Worldview series with circular error (CE90) and linear error (LE90) sequentially. "90" means that the minimum 90% of points measured have a geolocation error that is less than the stated value. The WV-4 images used in the study are stereo orthoready level 2A, and both CE90 and LE90

Downloaded From: https://www.spiedigitallibrary.org/journals/Journal-of-Applied-Remote-Sensing on 05 Jan 2022
Terms of Use: https://www.spiedigitallibrary.org/terms-of-use

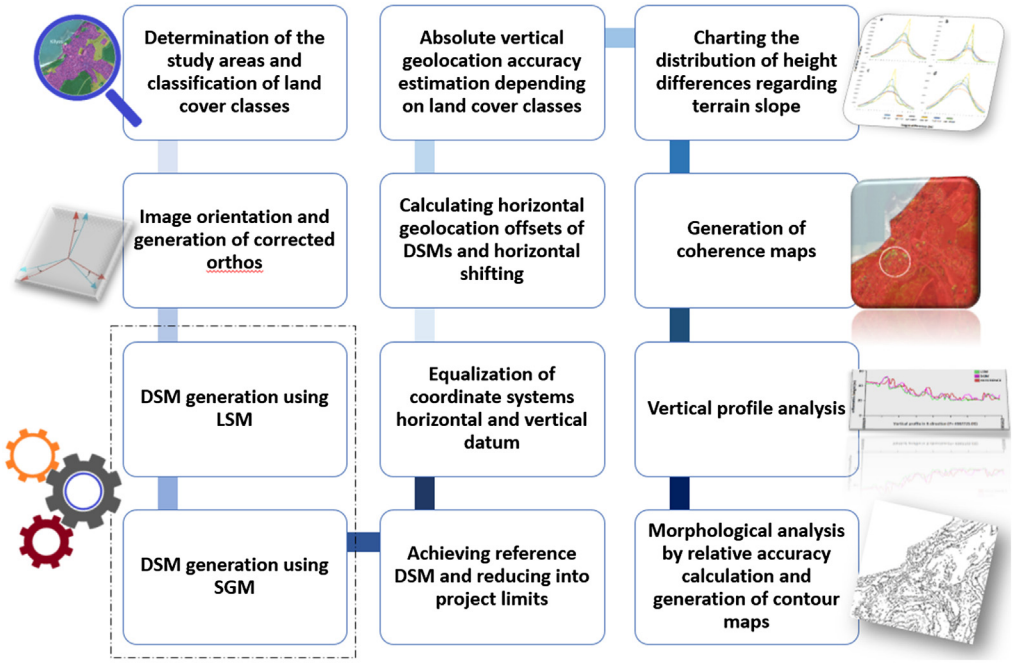

Fig. 3 Methodology steps.

were specified as <5 m by DigitalGlobe for <30 deg off-nadir view and excluding terrain slope. To generate high-accuracy large-scale mapping products from WV-4 imagery, inherently, the geometry needs to be improved, which is usual for high-resolution space-borne optical imagery.[26–28]

In this study, the bias-corrected sensor-oriented rational polynomial coefficient (RPC) model was used as the dominant method for high-resolution image orientation. The RPC model enables direct mapping from 3D object space coordinates (usually offset normalized latitude, longitude, and height) to 2D image coordinates (usually offset normalized line and sample values) by incorporating image shift and drift terms.[29–32] RPCs express the relationship between the image and the ground coordinates and are based on the satellite's direct sensor orientation using positioning systems, such as global positioning systems, gyros, and star sensors, which determine the attitude data.[33,34] Together with the images and the header data, the RPCs were distributed, and seven GCPs were established in the study area determined from 1/1000 scaled topographic vector maps generated from digital photogrammetry by the Istanbul Metropolitan Municipality. In three-dimensional image orientation, the resulting standard deviation is 0.5 pixel in X, 0.2 pixel in Y, and 0.9 pixels in Z. The accuracy of image orientation is shown in Table 1, and the error vector plots are presented in Fig. 4. In vector plots, the directions and the amounts of errors are not similar, demonstrating that the rectified ortho has no 3D systematic geolocation offset.

Table 1 The standard deviation of image orientation.

RPC orientation of single images			
Image	SX	SY	
Image 1	0.17 m (0.5 pixel)	0.09 m (0.3 pixel)	
Image 2	0.22 m (0.7 pixel)	0.25 m (0.8 pixel)	
Three-dimensional orientation			
Stereo model	SX	SY	SZ
	0.15 m (0.5 pixel)	0.07 m (0.2 pixel)	0.27 m (0.9 pixel)

Downloaded From: https://www.spiedigitallibrary.org/journals/Journal-of-Applied-Remote-Sensing on 05 Jan 2022
Terms of Use: https://www.spiedigitallibrary.org/terms-of-use

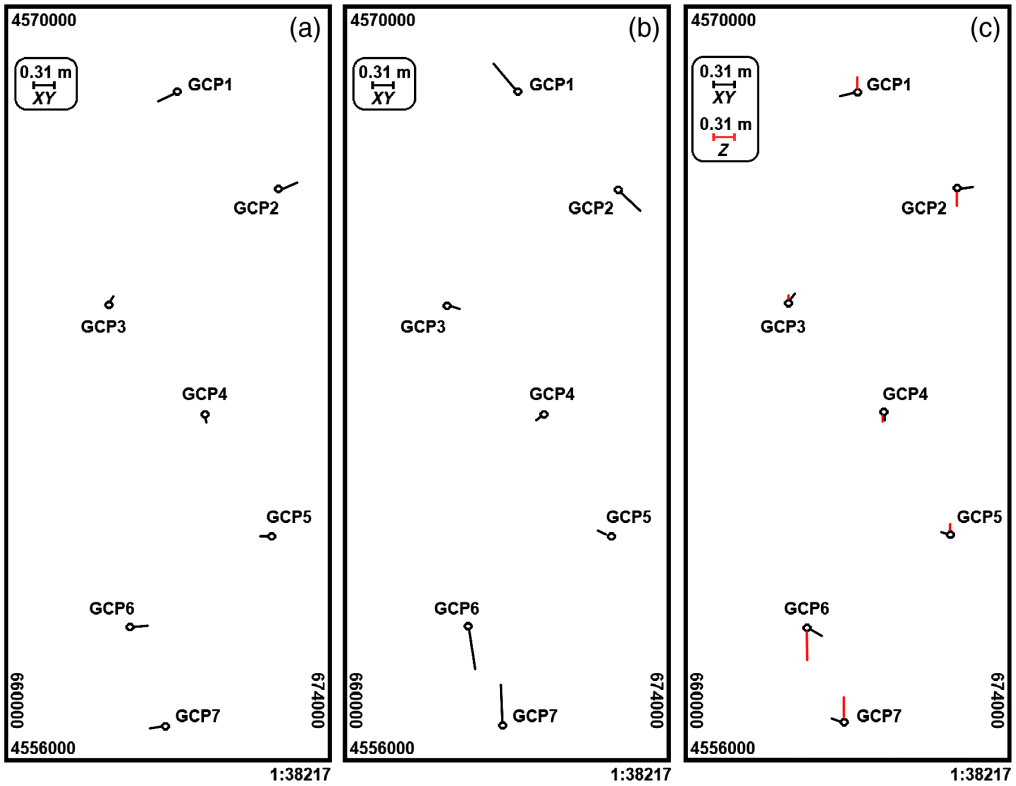

Fig. 4 (a), (b) The vector plots of the WV4 stereo imagery and (c) stereo model based on bias-corrected RPC orientation (m) (red is the differences in Z, and upward/downward directions mean ±).

3.2 *DSM Generation by Least Squares Matching and Semiglobal Matching*

In this study, one of the main objectives is to prove the effects of area-based LSM and pixel-based SGM algorithms on WV-4 DSM qualities. For high-quality DSM generation, accurate matching of the stereo images is crucial and depends on accurate image orientation. The image orientation accuracy should be <1 pixel; a lower accuracy leads to an increased number of wrong matches.[35] As shown in Table 1, orientation accuracy for the stereo model is 0.5 pixel in X, 0.25 pixel in Y, and 0.9 pixels in Z, which indicate a suitable condition for matching.

LSM has been one of the most preferred area-based image matching techniques in remote sensing since the 1980s. The basic principle of LSM is the geometric and radiometric matching of two or more image patches from a remotely sensed master image concerning a slave image.[36] In 1982, Foerstner[37] developed the LSM idea for a one-dimensional image line by integrating one translation parameter. Then the idea was adopted to the two-dimensional case by additional geometric and radiometric parameters using square or rectangular patches.[38–40] The method of LSM assumes that the best fit curve of a given type is the curve that has the minimal sum of deviations, which is the least squares error from a given set of data. It can be defined as creating a curve that best fits several data points.

On the other hand, the process of creating mathematical functions is known as curve fitting. For a given dataset, assembly curves of a particular type are generally not unique. The optimum curve can be obtained with the least-squares method, with minimum deviation from all data points. If the dataset points are assumed as $(x_1, y_1), (x_2, y_2), \ldots, (x_n, y_n)$ and x is an independent variable and y is a dependent variable, the connection curve $f(x)$ has the deviation (error) e_i from each data point as given in the following equation:

$$e_1 = y_1 - (x_1) \quad e_2 = y_2 - f(x_2) \quad \cdot \quad \cdot \quad e_n = y_n - f(x_n). \tag{2}$$

According to the LSM method, the equation of the best fit curve is given in Eq. (3). In this regard, the characteristic of the curve is minimal:

Downloaded From: https://www.spiedigitallibrary.org/journals/Journal-of-Applied-Remote-Sensing on 05 Jan 2022
Terms of Use: https://www.spiedigitallibrary.org/terms-of-use

$$\sum_{1}^{n} e_i^2 = \sum_{1}^{n} [y_i - f(x_i)]^2. \tag{3}$$

The SGM algorithm successfully combines the concepts of global and local stereo methods for accurate and pixel-wise matching at a low run time and estimates a dense disparity map from an oriented stereo image pair.[19,35,41] The key idea of SGM is to perform one-dimensional optimizations from all directions through the image regardless of sensor geometry. In the basic principle of SGM, two main components exist: matching cost computation and cost aggregation. The matching cost C (p, q) computes a similarity value for all potentially matching pixels in the image-pair utilizing the epipolar geometry.[42] In the computation, regularization is used for a proper reconstruction. For SGM, the matching step is cast into an energy minimization problem, and the discontinuity preserving energy is minimized with the following equation:

$$E(D) = \sum_{p} C(p, D_p) + \sum_{p,q \in N_p} V(D_p, D_q), \tag{4}$$

where

$$V(d, d') = \begin{cases} 0, & \text{if } d = d' \\ P1, & \text{if } |d - d'| = 1 \\ P2, & \text{otherwise} \end{cases}. \tag{5}$$

The matching cost function C takes a disparity map D that encodes the correspondences for each pixel location p in the first image and the other image. The pairwise term $V(p, q)$ penalizes disparity changes in the neighborhood N_p of each pixel location. The penalty $P1$ is added for all disparity changes equal to one pixel. At more significant discontinuities (disparity change >1 pixel), a fixed cost $P2$ is added. This cost function favors similar or slightly changing disparities between neighborhood pixels, thus stabilizing the matching in image areas with weak contrast and allowing large disparity jumps in areas with high contrast.[43] SGM can derive a suitable disparity for each pixel with spatial smoothness considered while spending reasonable run time proportional to the reconstructed volume.[44] Adjusting the time and finding the optimal disparity image is crucial for SGM.

Minimizing $E(D)$ in a two-dimensional manner is a very costly process, which is why SGM simplified the optimization by traversing one-dimensional paths and ensured the constraints with respect to these explicit directions. This approach requires a second phase known as cost aggregation.[45] In SGM, the minimization is realized by cost aggregation along a path in direction r as in the following equation:

$$L_r(p, d) = C(p, d) + \min_{d'}(L_r(p - r, d') + V(d, d')) - \min(L_r(p - r)). \tag{6}$$

Adding the costs L of paths in all directions r provides the aggregated cost S as given in the following equation:

$$S(p, d) = \sum_{r} L_r(p, d). \tag{7}$$

If a pixel adapts its disparity to the neighborhood, it may be assigned a lower cost for one direction. However, at least eight paths in the horizontal, vertical, and both diagonal orientations have to be introduced. If the number of paths is increased to 16, the streaking artifacts are reduced, and better results are achieved. The disparity map D is computed by identification of the minimum aggregated cost S for each pixel p in the first image.

The disparity image is transformed into the DSM with the desired projection and grid interval. In SGM DSM, the sharp object boundaries are achieved with the advantage of the sudden changeable depth at any pixel against area-based matching methods such as cross correlation, Fourier, mutual information, and optimization.[26,46] During the processes, the main disadvantage of SGM was the longer calculation time against LSM.

Downloaded From: https://www.spiedigitallibrary.org/journals/Journal-of-Applied-Remote-Sensing on 05 Jan 2022
Terms of Use: https://www.spiedigitallibrary.org/terms-of-use

SGM DSM was generated in PCI Geomatica software, and a reprojected epipolar stereo pair with a common orientation was required. Using an epipolar stereo pair, the possibility of incorrect matches was reduced. For increasing the accuracy of epipolar line alignment, which is very significant for generated DSM's quality, we used an epipolar tracking method. This method enables us to follow changes in the epipolar line over the stereo pair and automatically compensates for small gradual errors.

For the generation of WV-4 LSM DSM, DPLX and RAPORIO software, developed by Leibniz University Hannover, were used. The visualizations of the DSMs were done with the programs LISA and Surfer.

3.3 *DSM Validation*

The generated WV-4 DSMs by LSM and SGM were comprehensively analyzed by model-to-model visual and statistical approaches using a reference ALS DSM. The reference ALS DSM has 1 m grid spacing and covers the study area without any remarkable systematic errors, distortions, or gaps. Its geolocation accuracy was thoroughly investigated by comparing terrestrial laser scanning data in Ref. 47, and absolute horizontal and vertical geolocation standard deviations were presented as $\leq$6 and $\leq$25 cm, respectively. The ALS point cloud of the reference DSM was produced from 16 points/m^2 with flights organized by the Istanbul Metropolitan Municipality in 2013. The DSM is still actual in the study area because there is no significant change.

In DSM validation, the first stage should be the precorrections of the tested DSM and the reference. The coordinate system and horizontal and vertical datum have to be the same. In the study, Universal Transverse Mercator 35 deg (Istanbul) was used with World Geodetic System 1984 (WGS84) as the horizontal datum, and orthometric heights were preferred as the vertical datum. The other case is the 100% horizontal overlap of the tested DSM and the reference DSM for correct vertical accuracy validation. A horizontal offset between the models influences the height corresponding to Eq. (8) and causes misleading vertical accuracy results. Horizontal offsets were eliminated by shifting the analyzed DSMs to the reference DSM. In Eq. (8), DZ is the vertical discrepancy, DL is the horizontal offset, and α is the terrain slope:

$$DL = \frac{DZ}{\tan(\alpha)}. \tag{8}$$

After all precorrections, the vertical absolute and relative geolocation accuracies of WV-4 LSM and SGM DSMs were analyzed in three land cover classes: open, built-up, and forest, as shown in Fig. 5. The built-up areas are dominant in the study area with 50.14%. The land cover was classified by manual vectorization from VHR WV-4 orthoimage in NetCAD software.

In absolute vertical geolocation accuracy analysis, the standard deviation (STD_Z) and the normalized median absolute deviation ($NMAD_Z$) of height differences between WV-4 LSM and SGM DSMs and the reference was estimated by Eqs. (9) and (10), respectively. $NMAD_Z$ is the derivative of median absolute deviation (MAD_Z) of pixel height discrepancies between analyzed DSM and the reference and is very effective for the description of significant outliers. However, it is not as sensitive as STD_Z on large individual height differences. MAD_Z is normalized by a multiplication factor of 1.4826 to $NMAD_Z$ to reach the same probability of the STD_Z with

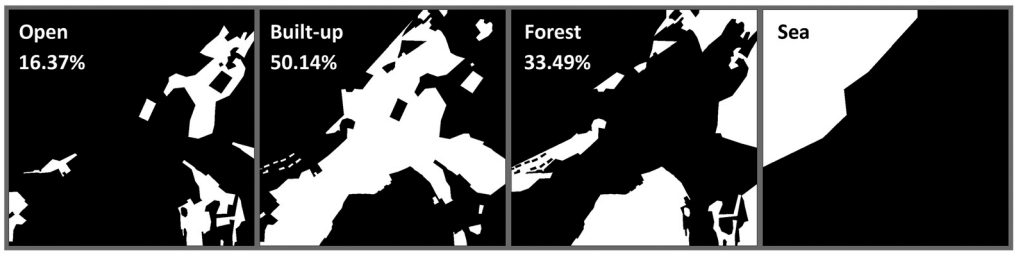

Fig. 5 Land cover classes in the study area.

Downloaded From: https://www.spiedigitallibrary.org/journals/Journal-of-Applied-Remote-Sensing on 05 Jan 2022
Terms of Use: https://www.spiedigitallibrary.org/terms-of-use

68.27% from 50% probability of MAD_Z. If the height differences are normal distributed, which means a symmetric distribution with a single peak (mode) in height distribution histogram, STD_Z and $NMAD_Z$ will be identical. In the forest and built-up areas, large discrepancies occur with the influence of the sudden height changes. In these cases, the normal distribution based on $NMAD_Z$ fits better to the frequency distribution of height differences in comparison with normal distribution based on STD_Z:

$$STD_Z = \sqrt{\frac{1}{n-1}\sum_{i=1}^{n}(\Delta Z_i - \mu)^2}, \tag{9}$$

$$NMAD_Z = 1.482615 \times m_i[|\Delta Z_i - \ m_{\Delta h}|], \tag{10}$$

where n is the number of height differences between analyzed DSM and the reference; ΔZ_i is the individual height differences (errors) between the analyzed and reference DSMs $i = 1, \ldots\ldots, n$; μ is the bias (arithmetic mean of the height differences); m_i is the median of the univariate data set of height discrepancies $i = 1, \ldots\ldots, n$; and $m_{\Delta h}$ is the median of absolute values of the height errors. Thus the $NMAD_Z$ is proportional to the median of the absolute differences between errors and the median error.[48]

In addition to STD_Z and $NMAD_Z$, skewness and kurtosis coefficients were analyzed in height distribution histograms. In a normal distribution, skewness and kurtosis coefficients should be around zero. Skewness indicates the lack of symmetry in the height distribution histogram. The negative skew coefficient refers to the pixel height difference distribution enlargement at the left side of the histogram peak, and the positive refers to the right side. Kurtosis is effective in the vertical direction of the height distribution histogram. In positive kurtosis, the histogram peak will be at the upward part of the normal distribution peak and indicates that the height differences between analyzed DSM and the reference mostly concentrate around one value; the negative kurtosis is at the downward part of the normal distribution peak. For the calculation of skewness and kurtosis, Eqs. (11) and (12) were used for an univariate data set of height discrepancies $(\Delta Z_1, \Delta Z_2, \Delta Z_3, \ldots., \Delta Z_n)$, where μ is the arithmetic mean and n is the number of pixels:

$$\text{skewness} = \frac{\sum_{i=1}^{n}(\Delta Z_i - \mu)^3/n}{{STD_Z}^3}, \tag{11}$$

$$\text{kurtosis} = \frac{\sum_{i=1}^{n}(\Delta Z_i - \mu)^4/n}{{STD_Z}^4}. \tag{12}$$

For visual interpretation of height errors between generated WV-4 DSMs and the reference ALS DSM by detecting erroneous regions (if available) and influence of land cover classes, color-coded height error maps (HEMs) were generated. HEMs are the differential models of analyzed and reference DSM and are basically calculated with Eq. (13). Empirically, the height error thresholds are used as ± 15 m ($\sim$3 times the standard deviation), which is the most suitable value to recognize the performances of LSM and SGM DSMs. In addition to HEMs, an arbitrary profile was detected in a 350-m section, and the vertical coherence of generated DSMs with reference was analyzed in the X direction:

$$HEM = DSM_{\text{reference}} - DSM_{\text{evaluated}}. \tag{13}$$

For demonstrating the morphologic performance of generated WV-4 DSMs, contour maps with 10 m equidistance were generated, and the relative standard deviation of height differences $RSTD_Z$ was estimated. The $RSTD_Z$ identifies the interior coherence between neighbor pixels on generated DSMs [Eq. (14)]. In this study, for each pixel of the generated DSMs, the distance ranges up to 10 pixel neighborhood ($1\,\text{m} \times 10 = 10\,\text{m}$) is used. n_Z indicates the number of point combinations in the distance group. A factor of 2 for multiplication with n_Z is used for normalization of the $RSTD_Z$ to STD_Z. If the height differences of the neighbored points are independent, corresponding to the error propagation, the $RSTD_Z$ would be the square root of 2.0 larger than STD_Z, which is given by $2 \times n_Z$:

Downloaded From: https://www.spiedigitallibrary.org/journals/Journal-of-Applied-Remote-Sensing on 05 Jan 2022
Terms of Use: https://www.spiedigitallibrary.org/terms-of-use

$$\mathrm{RSTD}_Z = \sqrt{\frac{\sum (\Delta Z_i - \Delta Z_j)^2}{2 \times n_Z}} \quad \text{computed for distance groups.} \tag{14}$$

The model-to-model statistical DSM validations were realized using Bundle Block Adjustment Leibniz University Hannover software. For HEM and morphological analysis, LISA software was utilized.

4 Results

As mentioned in Sec. 1, the effect of image matching algorithms on the final DSMs is crucial and a hot research topic for the scientific community. Accordingly, the visual and statistical comparison results of LSM and SGM on WV-4 DSM quality is given in this section. Figure 6 showed the reference ALS DSM and generated LSM and SGM WV-4 DSMs in the study area beside an instance region of interest (ROI) for better interpretation. As mentioned, the study area is dominant with buildings as 50%, and the superiority of SGM in the growing region is obvious compared with LSM in Fig. 6. The shapes of most buildings in SGM are very close to their actual shapes given in the ALS reference. In addition, linear details such as roads are depicted with high performance in SGM DSM.

In contrast to SGM, the area-based LSM was generated with subwindows of 10×10 pixels. Corresponding to such subwindows, it cannot describe buildings as well as the SGM; it shows small buildings as small hills. It requires contrast in the subwindows for matching. As a consequence, the description potential of building shapes in LSM is not at a sufficient level, considering the spatial resolution of WV-4 data. The linear details such as roads are available but shown with a noisy structure. In addition, some problems also stand out in open areas. The visual results in Fig. 6 confirm those in Ref. 20.

The absolute geolocation errors of LSM and SGM DSMs, calculated by the model-to-model comparison with the reference ALS, are shown in Tables 2 and 3, respectively. The detected and eliminated horizontal geolocation errors of the LSM and SGM DSMs are very close. In X direction, the horizontal geolocation errors are -0.12 m and -0.18 m for LSM and SGM respectively where $+0.11$ m and $+0.14$ m in Y direction. The absolute vertical geolocation accuracies in Table 3 were estimated for each land cover class separately regarding the effect of terrain slope. In addition to STD_Z and NMAD_Z, systematic vertical bias, skewness, and kurtosis values are given in this table. In the calculations, the points that have a >15 m height difference with the reference are excluded. Also the percentages of these points are shown in Table 3. In the absolute vertical accuracy assessment, the results in open areas are accepted as the most reliable by the scientific community because it does not change suddenly.[49] In Table 3, the performances of both LSM and SGM DSMs in open areas are higher than for other classes, as expected. In open areas, while the standard deviation of LSM DSM is ± 2.08 m and the NMAD_Z is ± 1.96 m, the SGM has an STD_Z of ± 0.98 m, and an NMAD_Z of ± 0.60 m. In flat terrain, without the influence of slope, the STD_Z reaches ± 1.46 m for LSM and ± 0.51 m for SGM DSMs, and the NMAD_Z reaches ± 1.42 m for LSM and ± 0.24 m for SGM DSMs. In open areas, kurtosis values also reach maximum levels because of the upward peak of the frequency distribution against the normal distribution.

In the built-up area, both DSMs declined in vertical absolute geolocation accuracy because of sudden height changes and the effect of buildings' vertical structure, which complicates the correct 3D determination from space depending on sensor viewing geometries with a height to base relation of 1:1.2. A smaller angle of convergence would have an advantage for matching in built-up areas. In most cases, a smaller angle of convergence generates a higher number of matching points in built-up areas, and a large angle of convergence causes a notably larger amount of missing data. Considering DSM completeness, occlusions are usually caused by larger convergence angles on the ground.[50,51] With a standard deviation of ± 1.88 and ± 1.12 m NMAD_Z, SGM DSM's performance is much better than LSM in built-up areas. Also most of the accuracy values for the LSM DSM are larger than SGM DSM in the forest.

In Fig. 7, histograms of height differences between generated DSMs and the reference ALS are given for open, built-up, and forest areas separately. In addition to the frequency distribution

Downloaded From: https://www.spiedigitallibrary.org/journals/Journal-of-Applied-Remote-Sensing on 05 Jan 2022
Terms of Use: https://www.spiedigitallibrary.org/terms-of-use

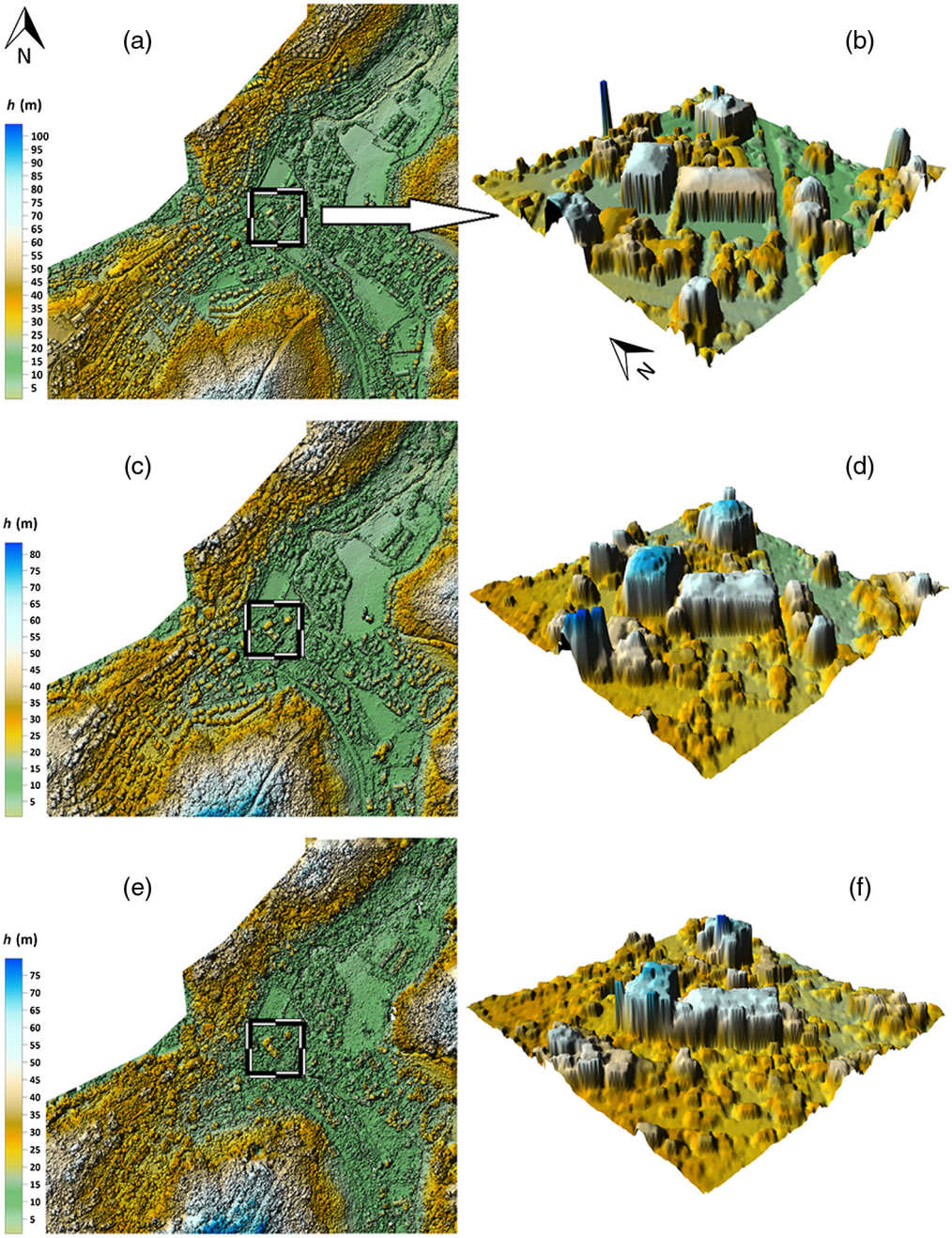

Fig. 6 (a) Reference ALS DSM, (b) reference ALS DSM ROI, (c) WV-4 SGM DSM, (d) WV-4 SGM DSM ROI, (e) WV-4 LSM DSM, and (f) WV-4 LSM DSM ROI.

Table 2 Estimated and eliminated horizontal geolocation offsets (errors).

Reference DSM	Area	Shifted DSM	ΔX (m)	ΔY (m)
ALS (1 m)	Kilyos	WV-4 LSM (1 m)	−0.12	0.11
		WV-4 SGM (1 m)	−0.18	0.14

Downloaded From: https://www.spiedigitallibrary.org/journals/Journal-of-Applied-Remote-Sensing on 05 Jan 2022
Terms of Use: https://www.spiedigitallibrary.org/terms-of-use

Table 3 Vertical geolocation accuracies of WV-4 LSM and SGM DSMs considering different land cover classes and the effect of terrain slope (α = slope).

Ref. DSM	Tested DSM	Land cover class	Bias (m)	STD_Z (bias eliminated) (m)		$NMAD_Z$ (bias eliminated) (m)		KURTOSIS (m)		SKEWNESS (m)		Excluded points (%) (>15 m)
				STD_Z	STD_Z $\alpha < 6$ deg	$NMAD_Z$	$NMAD_Z$ $\alpha < 6$ deg	$\alpha < 6$ deg		$\alpha < 6$ deg		
ALS (1 m)	WV-4 LSM (1 m)	Whole area 100%	−0.05	$3.07 + 0.41 \times \tan(\alpha)$	2.08	$2.29 + 0.60 \times \tan(\alpha)$	1.62	2.74	5.91	0.23	−1.14	0.53
		Open area 16.37%	−0.11	$2.08 + 0.20 \times \tan(\alpha)$	1.46	$1.96 + 0.20 \times \tan(\alpha)$	1.42	4.27	0.76	0.77	−0.23	0.29
		Built-up area 50.14%	0.13	3.39	2.34	$2.47 + 0.19 \times \tan(\alpha)$	1.58	2.72	5.67	0.15	−1.26	0.67
		Forest area 33.49%	−0.01	$3.25 + 0.69 \times \tan(\alpha)$	2.52	$2.63 + 0.88 \times \tan(\alpha)$	1.98	1.05	4.02	0.19	−1.07	1.21
	WV-4 SGM (1 m)	Whole area 100%	0.30	$1.62 + 0.42 \times \tan(\alpha)$	1.20	$0.98 + 0.56 \times \tan(\alpha)$	0.36	7.02	17.10	−0.73	−2.77	0.06
		Open area 16.37%	0.73	$0.98 + 0.29 \times \tan(\alpha)$	0.51	$0.60 + 0.38 \times \tan(\alpha)$	0.24	33.92	62.99	0.42	−4.48	0.26
		Built-up area 50.14%	0.31	$1.88 + 0.33 \times \tan(\alpha)$	1.50	$1.12 + 0.41 \times \tan(\alpha)$	0.48	6.65	13.17	−0.81	−2.78	0.22
		Forest area 33.49%	−0.13	$1.53 + 0.39 \times \tan(\alpha)$	1.22	$1.17 + 0.49 \times \tan(\alpha)$	0.49	4.05	6.14	−0.24	−1.16	0.28

Downloaded From: https://www.spiedigitallibrary.org/journals/Journal-of-Applied-Remote-Sensing on 05 Jan 2022
Terms of Use: https://www.spiedigitallibrary.org/terms-of-use

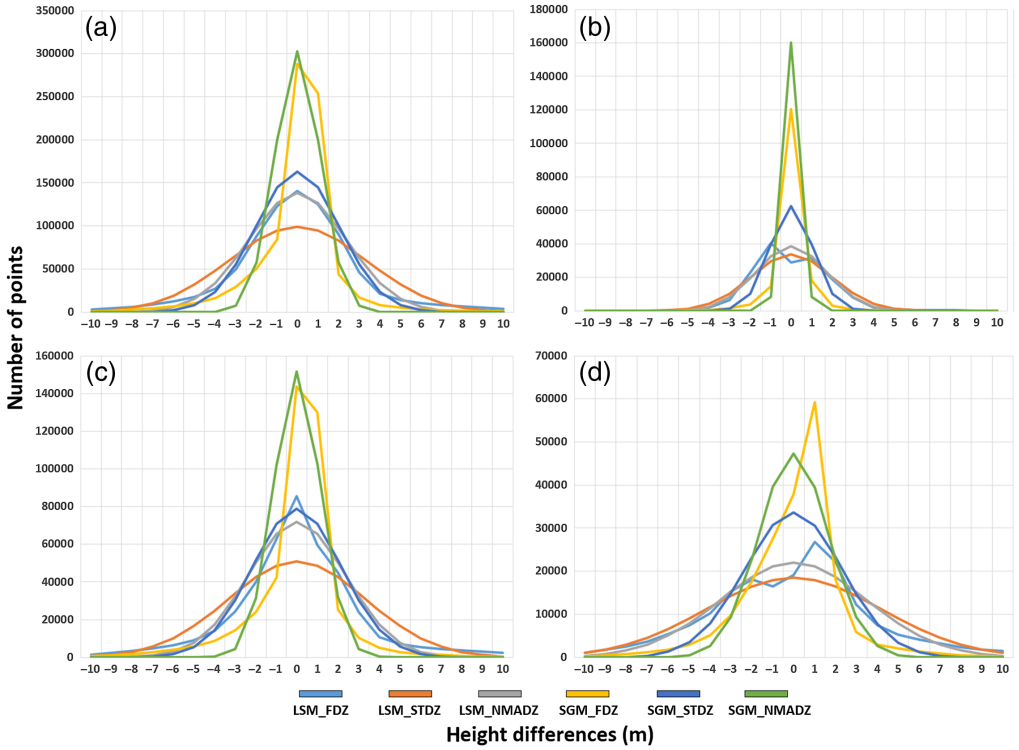

Fig. 7 Distribution of height differences between generated DSMs and reference ALS: (a) whole area, (b) open area, (c) built-up area, and (d) forest area.

of height differences (FD_Z), the normal distributions based on the STD_Z and $NMAD_Z$ are presented. The mentioned problem of LSM DSM against the reference DSM in open areas can be seen in the histogram. The frequency distribution of height errors has a double-peak around ± 1.5 m. A similar case is valid for LSM DSM in the forest. At least partially, this situation can be explained by the different descriptions of the forest surface by laser scanning and optical image matching. In all land classes, the better performance of SGM is precise.

Figure 8 shows the histograms of height differences for flat areas with an inclination below 5.7 deg (tangent < 0.1). In flat areas, the peaks of FD_Z and $NMAD_Z$ are much higher than for the normal distribution based on STD_Z for all of the land cover classes in SGM DSM. The normal distribution based on STD_Z is not as high in the center due to a higher percentage of larger discrepancies. In an open and flat area, the normal distribution based on STD_Z fits better to the frequency distribution in SGM. Except for forest, the modes of $NMAD_Z$ are higher than STD_Z and FD_Z in all land cover classes in SGM. In open and flat areas, the performance of SGM is maximum, which confirm the results in Table 3. On the other hand, LSM has double-peaks in open and forest regions.

Figure 9 shows the color coded HEMs of LSM and SGM DSMs provided with the height differences of corresponding pixels in the ALS reference. The error distribution histograms for ± 15 and 20 m height steps are given together with HEMs to interpret the effect of terrain inclination. In the HEMs, the height differences were estimated for all pixels; light green parts mean maximum coherence and minimum error, and the dark parts mean the lowest coherence and maximum error. In the HEMs, the topographic description potential differences between LSM and SGM are apparent. The SGM DSM looks more coherent with the reference against LSM, and the light green areas are dominant. On the other hand, LSM DSM has problems in every land class, in particular the errors reach up to 15 m in built-up and forest areas.

Figure 10 shows the vertical profile coherence in the X direction between LSM and SGM DSMs with the reference throughout a 350 m long cross section. As shown in this figure, different land cover classes are available in the cross section. In the open area on the left side, the profiles fit better together. In the built-up area, it has to be respected that the stereo scene has a height to base relation of 1:1.2. Corresponding to this in the orbit direction, the ground can only

Downloaded From: https://www.spiedigitallibrary.org/journals/Journal-of-Applied-Remote-Sensing on 05 Jan 2022
Terms of Use: https://www.spiedigitallibrary.org/terms-of-use

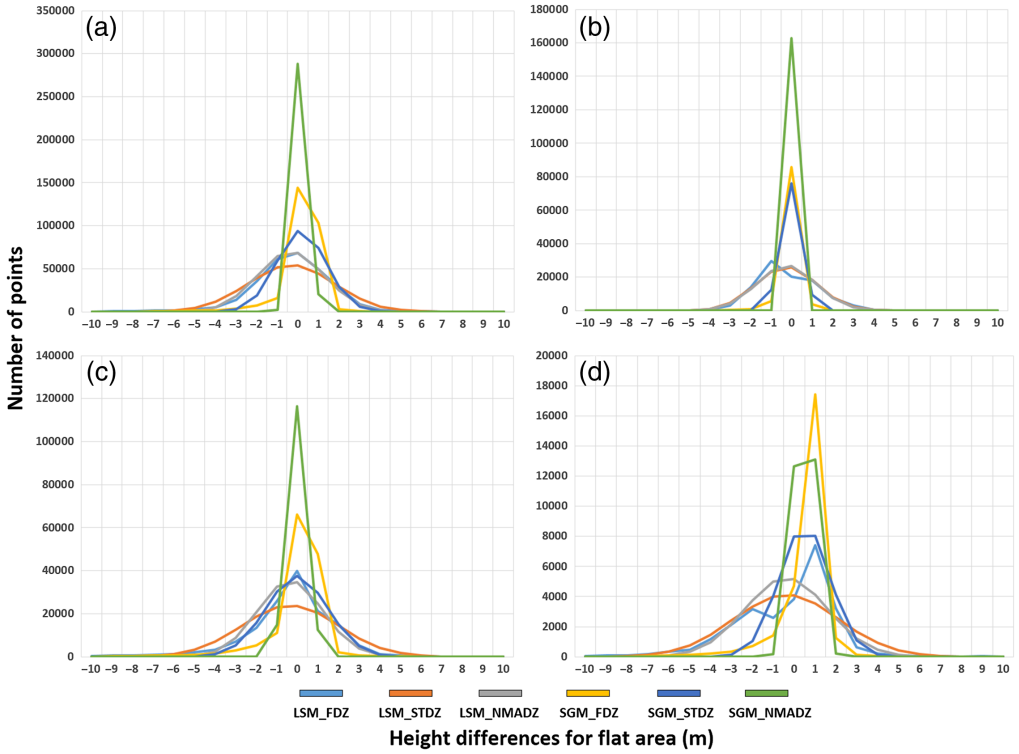

Fig. 8 Distribution of height differences between generated DSMs and reference ALS for uninclined areas: (a) whole area, (b) open area, (c) built-up area, and (d) forest area.

be seen stereoscopically if the distance between the buildings exceeds 83% of the building height, and this condition in most cases is not met. For LSM, not only a single pixel but also the larger part of the used matching window must be available stereoscopically. This situation explains why SGM DSM looks closer to the ALS profile in the vertical profiles compared with the LSM DSM.

Contour maps with 10 m equidistance and the relative vertical accuracies, as well as the morphologic performance indicators of generated WV-4 DSMs, are presented in Fig. 11 and Table 4. The contour lines of the DSM cannot be compared with the contour lines of the bare ground. In the DSM, the contour lines are going around most buildings, as the reference clearly shows. The LSM needs more free space around the building and cannot express vertical elements as the SGM. It explains the character of details in Fig. 11(a). Due to the height to base relation, the SGM has problems in showing the individual buildings. The high noise in a part of the contour lines of the reference is caused by vegetation. The $RSTD_Z$ performance of the SGM DSM pixels is better than that the LSM DSM in all land classes, similar to absolute accuracy. When interpreting the relative accuracy, it has to be respected that the definition of the DSM surface determined by ALS (first return) is not the same for matching by optical images.

5 Discussion of Results

In this section, the absolute vertical geolocation quality of generated WV-4 DSMs is discussed by comparing the results achieved from optical and synthetic aperture radar (SAR) satellites in previous reference studies of our research group in Istanbul. In accuracy, discussion regarding previous studies shows that the results in open areas are considered because of being the most reliable land cover class with a stable structure independent of the study area.

In Ref. 15, DSM has been generated with WV-2 stereo pairs in northern Istanbul and comprehensively analyzed with the model-to-model-based approaches using different reference DSMs. The standard deviation of the height based on WV-2 [0.5 m ground sampling distance (GSD)] reached ± 1.93 m against an ALS reference DSM in that study. Table 5 shows the

Downloaded From: https://www.spiedigitallibrary.org/journals/Journal-of-Applied-Remote-Sensing on 05 Jan 2022
Terms of Use: https://www.spiedigitallibrary.org/terms-of-use

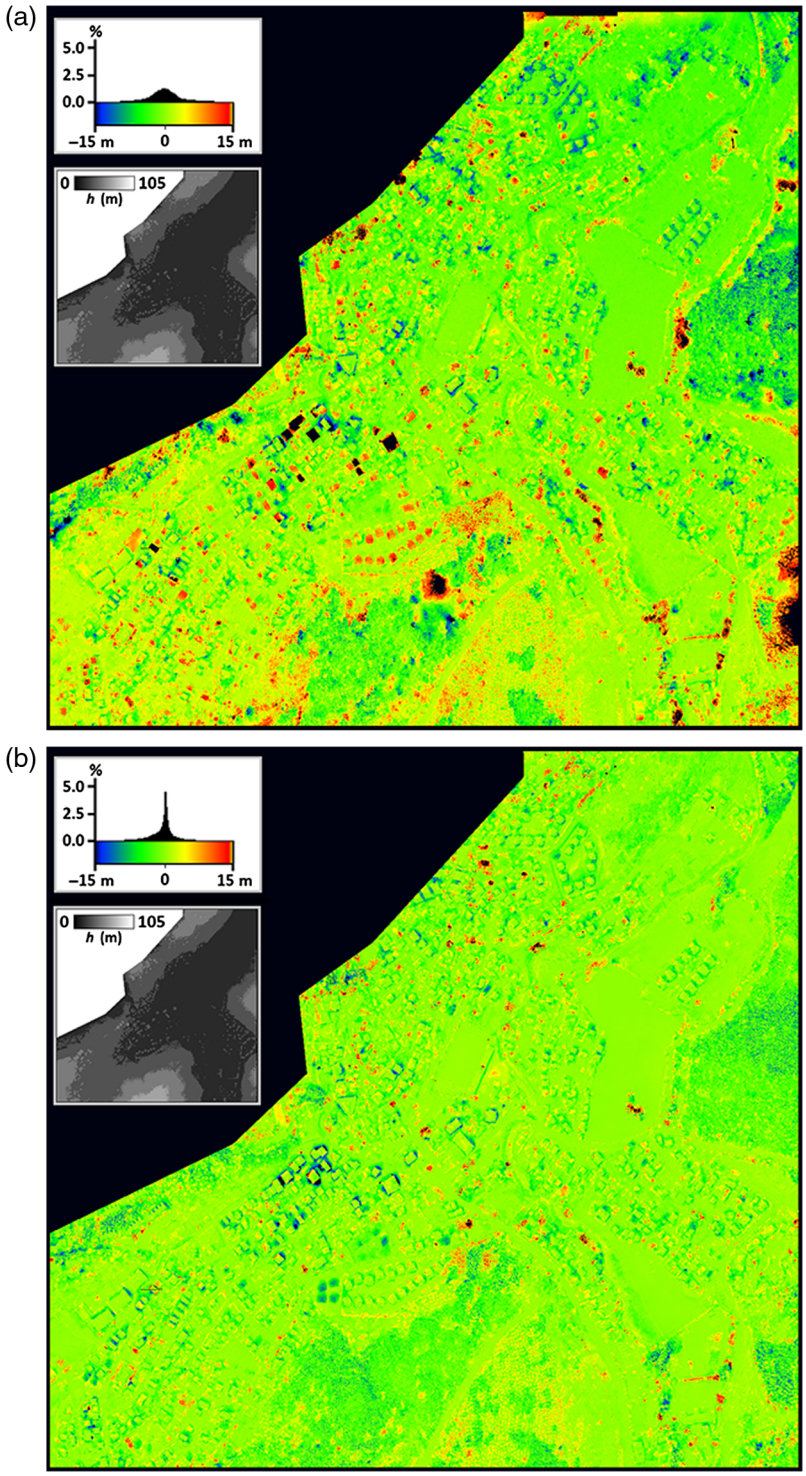

Fig. 9 Generated HEMs overlapped: (a) LSM DSM and (b) SGM DSM.

standard deviation of height of the optical and SAR satellites that our research group achieved in Istanbul approaching, in comparisons, the same ALS reference DSM used in this study.

In Table 5, it is clear that the absolute vertical geolocation accuracy of WV-4 SGM DSM is the highest in compared with other optical and SAR satellites' DSMs in Istanbul. However, Table 5 also demonstrates that the accuracy is not linear depending on the GSD; it also strongly depends on morphologic details (see Fig. 11), which are more complicated with higher ground

Downloaded From: https://www.spiedigitallibrary.org/journals/Journal-of-Applied-Remote-Sensing on 05 Jan 2022
Terms of Use: https://www.spiedigitallibrary.org/terms-of-use

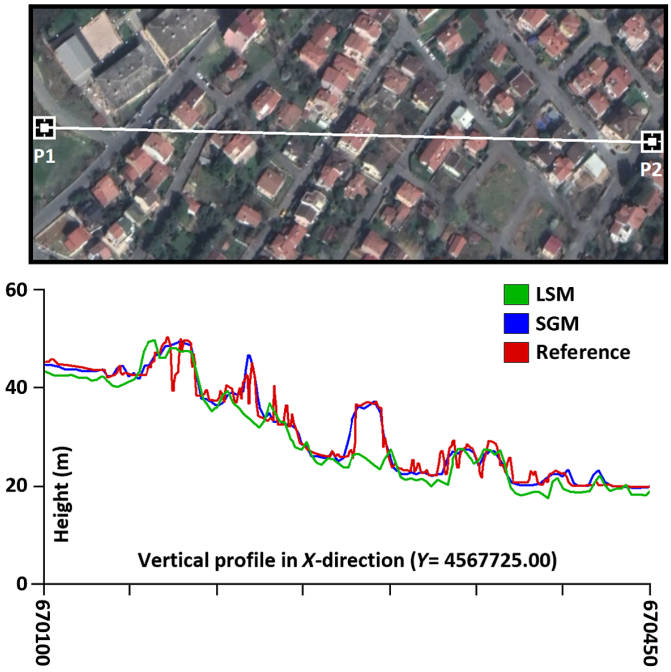

Fig. 10 Vertical profile over 350 m of ALS reference and evaluated DSMs.

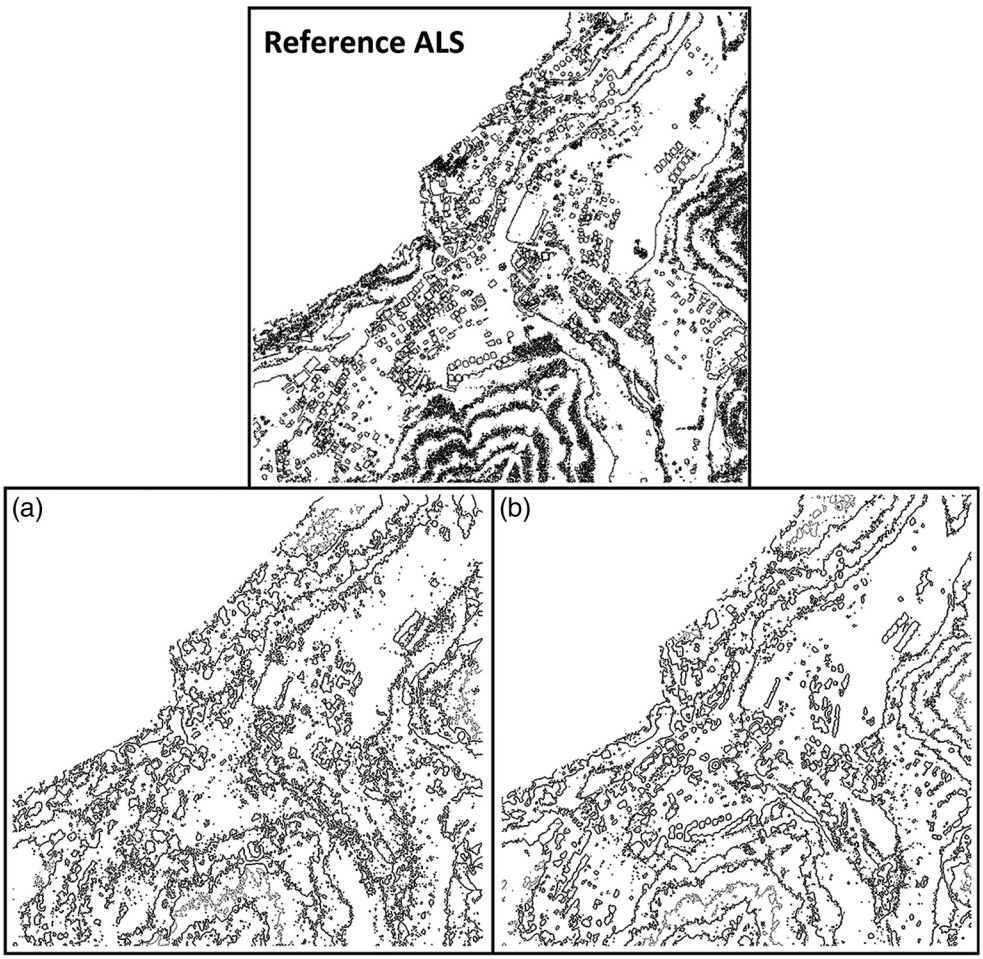

Fig. 11 Morphological case: (a) 10 m interval contour lines generated from LSM and (b) 10 m interval contour lines generated from SGM.

Downloaded From: https://www.spiedigitallibrary.org/journals/Journal-of-Applied-Remote-Sensing on 05 Jan 2022
Terms of Use: https://www.spiedigitallibrary.org/terms-of-use

Table 4 The relative vertical standard deviation of tested DSMs as a function of point distance.

		$RSTD_Z$ (m)							
		WV-4 LSM				WV-4 SGM			
Ref. DSM	Distance (10 m)	Whole	Open	Built up	Forest	Whole	Open	Built up	Forest
ALS (1 m)	1	1.40	0.78	1.47	1.79	1.12	0.64	1.19	1.40
	2	1.86	0.99	1.98	2.33	1.44	0.80	1.56	1.74
	3	2.15	1.11	2.29	2.66	1.62	0.88	1.76	1.91
	4	2.34	1.18	2.51	2.87	1.72	0.93	1.88	2.01
	5	2.48	1.23	2.66	3.03	1.79	0.97	1.96	2.06
	6	2.59	1.26	2.78	3.14	1.83	0.99	2.01	2.10
	7	2.67	1.28	2.86	3.23	1.87	1.00	2.05	2.13
	8	2.73	1.29	2.92	3.29	1.89	1.01	2.08	2.16
	9	2.77	1.30	2.97	3.34	1.92	1.02	2.10	2.18
	10	2.80	1.31	3.00	3.38	1.93	1.03	2.12	2.20

Table 5 Absolute vertical geolocation accuracies of different satellites' DSMs.

Study area	Reference DSM	Analyzed DSM	GSD (m)	DSM spacing (m)	STD_Z (m)	STD_Z (GSD)	Reference study
Istanbul	ALS	WV-4 SGM	0.30	1	0.51	1.7	This study
	ALS	WV-4 LSM	0.30	1	1.46	4.9	This study
	ALS	WV-2	0.50	1	1.93	3.9	15
	ALS	ALOS AW3D30	2.5	30	4.89	2.0	52
	ALS	KOMPSAT-3	0.70	5	2.80	4.0	53
	ALS	SRTM X-band	20 × 30	30	5.36	SAR	52
	ALS	TerraSAR-X HS	1	2	8.04	SAR	54
	ALS	Cosmo-SkyMed HS	1	2	8.51	SAR	54
	ALS	Sentinel-1A IW	5 × 20	15	5.07	SAR	52

resolution. In the densely built-up area of Istanbul city, SAR has problems with layover and imaging shadows, which is why the performance of SAR DSMs is not as high as optical DSMs.

6 Conclusion

In this study, the topographic description potential of the latest VHR WV-4 optical satellite was investigated with visual and statistical approaches. The WV-4 DSMs were generated by least squares and by SGM algorithms separately and evaluated against an ALS reference model. The effects of LSM and SGM algorithms on DSM quality were analyzed in detail. The analysis took place in the Kilyos district, located in the Istanbul Metropolitan Municipality. The test area has a rough topographic structure, and the three different land cover classes are open, built-up, and forest. The built-up areas are dominant with 50% of the area. To demonstrate the influence of terrain slope on WV-4 DSM quality, the analysis was done separately for the whole area and flat areas (<5.7 deg inclination).

Downloaded From: https://www.spiedigitallibrary.org/journals/Journal-of-Applied-Remote-Sensing on 05 Jan 2022
Terms of Use: https://www.spiedigitallibrary.org/terms-of-use

The statistical results of absolute and relative vertical quality assessment and visual analysis demonstrated that the SGM technique is more accurate and includes more details than LSM for DSM generation with VHR space-borne optical data in urban areas. The horizontal geolocation performances of both DSMs are high and around ±0.3 to 0.6 pixels. The absolute vertical geolocation accuracy of WV-4 SGM DSM reaches up to ±0.51 m (1.7 pixels) as STD_Z and ±0.24 m (0.8 pixels) as $NMAD_Z$ in open and flat areas, whereas LSM DSM is limited with ±1.46 (4.9 pixels) and ±1.42 m (4.7 pixels), respectively. The absolute vertical accuracy of SGM DSM is the highest value that our research group achieved from an optical space-borne mission. In addition, relative accuracies of the WV-4 SGM DSM are very high, particularly in open areas. Generated HEMs prove that LSM DSM is not as accurate as SGM in all land cover classes and flat topography. According to the HEMs and vertical profiles in the 350 m cross section, WV-4 SGM DSM looks very close to the reference ALS DSM, which supports the numerical results.

Acknowledgments

We would like to thank Yıldız Technical University for supporting the acquisition of WV-4 stereo imagery in the scope of the Scientific Research Project with ID: 3075. In addition, many thanks to the Istanbul Metropolitan Municipality for reference ALS data.

References

1. A. El Garouani and A. Alobeid, "Digital surface model generation for 3D City modeling (Fez, Morocco), 8th National GIS Symposium in Saudi Arabia," in The Road for Building Saudi Arabia GIS organized by the high Committee of the GIS at the Eastern Province, Dammam, Saudi Arabia, April 15–17 (2013).
2. M. Font, D. Amorese, and H. L. Lagarde, "DEM and GIS analysis of the stream gradient index to evaluate effects of tectonics: the Normandy intraplate area (NW France)," *Geomorphology* **119**(3–4), 172–180 (2010).
3. U. G. Sefercik et al., "Novel fusion approach on automatic object extraction from spatial data: case study Worldview-2 and TOPO5000," *Geocarto Int.* **33**(10), 1139–1154 (2018b).
4. R. R. Navalgund, V. Jayaraman, and P. S. Roy, "Remote sensing applications: an overview," *Curr. Sci.* **93**(12), 1747–1766 (2007).
5. U. G. Sefercik and A. Atesoglu, "Three-dimensional forest stand height map production utilizing airborne laser scanning dense point clouds and precise quality evaluation," *iForest* **10**, 491–497 (2017).
6. D. Tapete and F. Cigna, "COSMO-SkyMed SAR for detection and monitoring of archaeological and cultural heritage sites," *Remote Sens.* **11**, 1326 (2019).
7. M. Alkan et al., "Geometric accuracy and information content of Worldview-1 images," *Opt. Eng.* **52**(2), 026201 (2013).
8. D. Poli et al., "Radiometric and geometric evaluation of GeoEye-1, Worldview-2 and Pleiades-1A stereo images for 3D information extraction," *ISPRS J. Photogramm. Remote Sens.* **100**, 35–47 (2015).
9. F. Hu et al., "DEM extraction from Worldview-3 stereo-images and accuracy evaluation. ISPRS," *Int. Arch. Photogramm. Remote Sens. Spatial Inf. Sci.* **XLI-B1**, 327–332 (2016).
10. T. Wang and A. Gruen, "Georeferencing accuracy analysis of Worldview-2 and IKONOS images of Singapore based on RPFs," in *33rd Asian Conf. Remote Sens. (ACRS)*, pp. 1494–1501 (2012).
11. T. Toutin, C. V. Schmitt, and H. Wang, "Impact of no GCP on elevation extraction from Worldview stereo data," *ISPRS J. Photogramm. Remote Sens.* **72**, 73–79 (2012).
12. M. Crespi et al., "A new rigorous model for high resolution satellite imagery orientation: application to EROS A and QuickBird," *Int. J. Remote Sens.* **33**(8), 2321–2354 (2012).
13. D. Poli, K. Wolff, and A. Gruen, "Evaluation of Worldview-1 stereo scenes and related 3D products," *Int. Arch. Photogramm. Remote Sens. Spatial Inf. Sci.* **XXXVIII-1-4-7/W5**, 1–6 (2008).

Downloaded From: https://www.spiedigitallibrary.org/journals/Journal-of-Applied-Remote-Sensing on 05 Jan 2022
Terms of Use: https://www.spiedigitallibrary.org/terms-of-use

14. K. Jacobsen, "DEM generation from high resolution satellite imagery," *Fernerkund. Photogramm.* **2013**, 483–493 (2013).
15. U. G. Sefercik et al., "Generation and validation of high-resolution DEMs from Worldview-2 stereo data," *Photogramm. Rec.* **28**(144), 362–374 (2013).
16. O. R. Belfiore and C. Parente, "Comparison of different algorithms to orthorectify Worldview-2 satellite imagery," *Algorithms* **9**(4), 67 (2016).
17. M. A. Aguilar et al., "Quality assessment of digital surface models extracted from Worldview-2 and Worldview-3 stereo pairs over different land covers," *GIScience Remote Sens.* **56**(1), 109–129 (2019).
18. Z. Li and J. Wang, "Least squares image matching: a comparison of the performance of robust estimators," *ISPRS Ann. Photogramm. Remote Sens. and Spatial Inf. Sci.* **II-1**, 37–44 (2014).
19. H. Hirschmuller, "Accurate and efficient stereo processing by semi-global matching and mutual information," in *Proc. IEEE Conf. CVPR*, New York (2005).
20. A. Alobeid et al., "Building monitoring with differential DSMs," *ISPRS Hannover Workshop, Int. Arch. Photogramm. Remote Sens.* **XXXVIII-4(W19)**, 7–16 (2011).
21. L. Zhang and A. Gruen, "Multi-image matching for DSM generation from IKONOS imagery," *ISPRS J. Photogramm. Remote Sens.* **60**(3), 195–211 (2006).
22. J. Hua, J. Zhou, and W. Yang, "Comparing LiDAR and SFM digital surface models for three land cover types," *Open Geosci.* **13**, 497–504 (2021).
23. G. Kateřina, M. Jana, and M. Vítězslav. "Accuracy assessment of the global TanDEM-X digital elevation model in a mountain environment," *Remote Sens. Environ.* **241**, 111724 (2020).
24. G. Colosimo et al., "Accuracy evaluation of SRTM and ASTER DSMs," in *29th Annu. EARSeL Symp.*, Chania, Crete (2009).
25. A. Alobeid, K. Jacobsen, and C. Heipke, "Building height estimation in urban areas from very high resolution satellite stereo images," in *ISPRS Hannover Workshop, Int. Arch. Photogramm. and Remote Sens.*, Vol. XXXVIII-1-4-7/W5, pp. 2–5 (2009).
26. C. Heipke, "Automation of interior, relative, and absolute orientation," *ISPRS J. Photogramm. Remote Sens.* **52**, 1–19 (1997).
27. G. Buyuksalih, M. Oruc, and K. Jacobsen, "Precise georeferencing of rectified high resolution space images," in *XXth ISPRS Congr.*, Istanbul, Vol. 35, pp. 184–188 (2004).
28. T. Toutin, "Geometric processing of remote sensing images: models, algorithms and methods," *Int. J. Remote Sens.* **25**, 1893–1924 (2004).
29. C. S. Fraser and H. B. Hanley, "Bias-compensated RPCs for sensor orientation of high-resolution satellite imagery," *Photogramm. Eng. Remote Sens.* **71**(8), 909–915 (2005).
30. J. Grodecki, "IKONOS stereo feature extraction: RPC approach," in *ASPRS Annu. Conf., St. Louis* (2001).
31. J. Grodecki and D. Gene, "Block adjustment of high-resolution satellite images described by rational polynomials," *Photogramm. Eng. Remote Sens.* **69**(1), 59–68 (2003).
32. I. Najafi and M. Momeni, "Precision evaluation of RPCs in HRSI orientation of Geoeye-1," in *5th Symp. Adv. and Sci. and Technol.*, Mashhad (2011).
33. C. S. Fraser and H. B. Hanley, "Bias compensation in rational functions for IKONOS satellite imagery," *Photogramm. Eng. Remote Sens.* **69**(1), 53–57 (2003).
34. K. Di, R. Ma, and R. Li, "Rational functions and potential for rigorous sensor model recovery," *Photogramm. Eng. Remote Sens.* **69**(1), 33–41 (2003).
35. H. Hirschmüller and T. Bucher, "Evaluation of digital surface models by semi-global matching," in *DGPF*, Vienna (2010).
36. F. Bethmann and T. Luhmann, "Least-squares matching with advanced geometric transformation models," *Int. Arch. Photogramm. Remote Sens. Spatial Inf. Sci.* **38**(Part 5), 86–91 (2010).
37. W. Foerstner, "On the geometric precision of digital correlation," *Int. Arch. Photogramm. Remote Sens.* **24**(3), 176–189 (1982).
38. F. Ackermann, "Digital image correlation: performance and potential in photogrammetry," *Photogramm. Rec.* **11**(64), 429–439 (1984).
39. A. Pertl, "Digital image correlation with the analytical plotter Planicomp C-100," *Int. Arch. Photogramm. Remote Sens.* **25**(3B), 874–882 (1984).
40. A. Grun, "Adaptive least-squares correlation: a powerful image matching technique," *South Afr. J. Photogramm. Remote Sens. Cartograph.* **14**(3), 175–187 (1985).

Downloaded From: https://www.spiedigitallibrary.org/journals/Journal-of-Applied-Remote-Sensing on 05 Jan 2022
Terms of Use: https://www.spiedigitallibrary.org/terms-of-use

41. H. Hirschmüller, "Stereo processing by semi-global matching and mutual information," *IEEE Trans. Pattern Anal. Mach. Intell.* **30**, 328–341 (2008).
42. H. Hirschmüller and D. Scharstein, "Evaluation of stereo matching costs on image with radiometric differences," *IEEE Trans. Pattern Anal. Mach. Intell.* **31**(9), 1582–1599 (2009).
43. P. D'angelo, "Improving semi-global matching: cost aggregation and confidence measure," *ISPRS Int. Arch. Photogramm. Remote Sens. Spatial Inf. Sci.* **XLI-B1**, 299–304 (2016).
44. P. D'angelo and P. Reinartz, "Semi-global matching results on the ISPRS stereo matching benchmark," *ISPRS Int. Arch. Photogramm. Remote Sens. Spatial Inf. Sci.* **XXXVIII-4/W19**, 79–84 (2011).
45. M. Michael et al., "Real-time stereo vision: optimizing semi-global matching," in *IEEE Intell. Veh. Symp. (V)* (2013).
46. J. Joglekar and S. S. Gedam, "Area based image matching methods: a survey," *Int. J. Emerg. Technol. Adv. Eng.* **2**, 130–136 (2012).
47. U. G. Sefercik et al., "Point-based and model-based geolocation analysis of airborne laser scanning data," *Opt. Eng.* **56**(1), 013101 (2017).
48. J. Höhle and M. Höhle, "Accuracy assessment of digital elevation models by means of robust statistical methods," *ISPRS J. Photogramm. Remote Sens.* **64**(4), 398–406 (2009).
49. U. G. Sefercik et al., "Area-based quality control of airborne laser scanning 3D models for different land classes using terrestrial laser scanning: sample survey in Houston, USA," *Int. J. Remote Sens.* **36**(23), 5916–5934 (2015).
50. L. Piermattei, et al., "Impact of the acquisition geometry of very high-resolution Pléiades imagery on the accuracy of canopy height models over Forested Alpine regions," *Remote Sens.* **10**(10), 1542 (2018).
51. A. Loghin, J. Otepka-Schremmer, and N. Pfeifer, "Potential of Pléiades and Worldview-3 Tri-stereo DSMs to represent heights of small isolated objects," *Sensors* **20**(9) 2695.
52. U. G. Sefercik et al., "Validation of Sentinel-1A and AW3D30 DSMs for the metropolitan area of Istanbul, Turkey," *J. Photogramm. Remote Sens. Geoinf. Sci.* **86**(3–4), 141–155 (2018).
53. U. G. Sefercik et al., " DSM quality of Korean satellite KOMPSAT-3 in comparison to AW3D30 and Sentinel-1A in respect of airborne laser scanning," *KSCE J. Civil Eng.* **23**(7), 3162–3173 (2019).
54. U. G. Sefercik and N. Yastikli, "ALS Model-based comparison of Cosmo-SkyMed and TerraSAR-X HS DSMs on varied land forms," *J. Spatial Sci.* **61**(1), 119–131 (2016).

Umut G. Sefercik received his MSc degree and PhD in geomatics from Zonguldak Bülent Ecevit University in 2006 and 2010, respectively. He finished his postdoctoral at the National Center for Airborne Laser Mapping (NCALM), University of Houston, Texas, USA, in 2014. He is a professor at Gebze Technical University. He is the author of more than 20 SCI journal papers. His research interests are processing, generation, and quality validation of airborne and space-borne remote sensing data and products.

Mehmet Alkan received his MSc degree and PhD in geomatics from Karadeniz Technical University 1997 and 2005, respectively. He is a professor at Yıldız Technical University. He is the author of more than 25 SCI journal papers and has written a book chapter. His research interests are database management, geographical information systems, remote sensing, object extraction, national spatial data infrastructure, e-municipality, and e-government.

Karsten Jacobsen received his PhD in photogrammetry from Leibniz University Hannover, Hannover, Germany. He is an expert on digital photogrammetry and space-borne remote sensing.

Can Atalay received his MSc degree from Zonguldak Bülent Ecevit University in 2017. He is continuing his doctoral studies and is a research assistant in the Geomatics Engineering Department at Zonguldak Bülent Ecevit University

Gurcan Buyuksalih received his PhD from the Department of Geography and Topographic Science, University of Glasgow, Glasgow, UK. He is an associate professor in photogrammetry at Private Sector, Istanbul, Turkey. His research direction is the full range of photogrammetry and remote sensing.

Downloaded From: https://www.spiedigitallibrary.org/journals/Journal-of-Applied-Remote-Sensing on 05 Jan 2022
Terms of Use: https://www.spiedigitallibrary.org/terms-of-use